Mass-Loss Timescale of Star Clusters
in an External Tidal Field.
II. Effect of Mass Profile of Parent Galaxy

Ataru TANIKAWA[1,2] and Toshiyuki FUKUSHIGE[1,3]

[1] *Department of General System Studies, College of Arts and Sciences,*
University of Tokyo, 3-8-1 Komaba, Meguro-ku, Tokyo 153-8902
[2] *Center for Computational Sciences, University of Tsukuba,*
1-1-1 Tennodai, Tsukuba, Ibaraki 305-8577
[3] *K&F Computing Research Co., Chofu, Tokyo 182-0026*

tanikawa@ccs.tsukuba.ac.jp

Abstract

We investigate the long-term dynamical evolution of star clusters in a steady tidal field produced by its parent galaxy. In this paper, we focus on the influence of mass profile of the parent galaxy. The previous studies were done with the simplification where the parent galaxy was expressed by point mass. We express different mass profiles of the parent galaxy by the tidal fields in which the ratios of the epicyclic frequency κ to the angular velocity ω are different. We compare the mass-loss timescale of star clusters whose tidal radii are identical but in parent galaxies with different mass profile, by means of orbits calculations in fixed cluster potential and N-body simulations. In this situation, a cluster rotates around the parent galaxy more rapidly as the parent galaxy has shallower mass profile. We found that the mass-loss timescale increase 20% and 50% for the cases that the mass density profile of the parent galaxies are proportional to R^{-2} and $R^{-1.5}$ where R is the distance from the galaxy center, compared to the point-mass case, in moderately strong tidal field. Counterintuitively, a cluster which rotates around the parent galaxy more rapidly has a longer lifetime. The increase of lifetime is due to the fact that the fraction occupied by regular-like orbit increases in shallower profile. Finally, we derive an evaluation formula for the mass-loss timescale of clusters. Our formula can explain a property of the population of the observed galactic globular clusters that their half-mass radii become smaller as their distances from the galactic center become smaller.

Key words: celestial mechanics — star clusters — stellar dynamics

Table 1. Relation among mass density profiles of galaxies, the angular velocities of the clusters, and the epicyclic frequency.

$\rho \propto R^{-\infty}$(point mass)	$\omega \propto R^{-3/2}$	$\kappa^2 = \omega^2$
$\rho \propto R^{-2}$	$\omega \propto R^{-1}$	$\kappa^2 = 2\omega^2$
$\rho \propto R^{-1.5}$	$\omega \propto R^{-3/4}$	$\kappa^2 = (5/2)\omega^2$
$\rho \propto R^{-1}$	$\omega \propto R^{-1/2}$	$\kappa^2 = 3\omega^2$
$\rho \propto R^0$	$\omega \propto R^0$	$\kappa^2 = 4\omega^2$

1. Introduction

In a star cluster, stars exchange their energy with the other stars through their encounters, and the whole system approaches to thermodynamically relaxed state. This process is called two-body relaxation. In this process, some stars have high energy enough to escape from the cluster and the system loses its mass. Therefore, the mass-loss timescale of a cluster is thought to be proportional to its two-body relaxation time (Ambartsumian 1938; Spitzer 1940).

However, this is not true for a cluster in an external tidal field, which was first shown by means of N-body simulations in the Collaborative Experiment (Heggie et al. 1998). Fukushige and Heggie (2000) (hereafter, FH) showed that stars which have enough energy to escape from the cluster (hereafter, "potential escapers") can remain inside the cluster before finding exits on timescale comparable to the two-body relaxation time of the cluster, and that the timescale (hereafter, "escape time delay") complicates the scaling of mass-loss timescale with two-body relaxation time. Baumgardt (2001) and Baumgardt and Makino (2003) performed N-body simulations in the external tidal field, and found the mass-loss timescale are proportional to the half-mass relaxation time to the power of $3/4$. Tanikawa and Fukushige (2005) (hereafter, paper I) also performed N-body simulations, and found that the power depends on the strength of the tidal field and the power $3/4$ shown by Baumgardt (2001) can be observed in the case of moderately strong tide. These findings mean that for treatment of mass loss of clusters in the external tidal field, it is desirable for orbits of stars to be fully resolved, and N-body simulation is more appropriate than orbit-averaged method, such as Fokker-Planck method.

This is a succeeding paper of Paper I. In this paper, we investigate the effect of the mass profile of the parent galaxy which produces the tidal field. In most of previous simulations of star clusters with the external tidal field (Giersz, Heggie 1994; McMillan, Hut 1994; Fukushige, Heggie 1995; Baumgardt 2001; Paper I; Trenti et al. 2007), the parent galaxy are simplified as point mass.

If we consider the mass profile of the parent galaxy, the equations of motion of star clusters moving in the circular orbit around the galaxy are expressed, with tidal approximation, as

$$\frac{d^2\mathbf{r}_i}{dt^2} = -2 \begin{pmatrix} 0 \\ 0 \\ \omega \end{pmatrix} \times \frac{d\mathbf{r}_i}{dt} - \begin{pmatrix} (\kappa^2 - 4\omega^2)x_i \\ 0 \\ \nu^2 z_i \end{pmatrix} - \nabla\Phi_{c,i}, \tag{1}$$

where ω is a angular velocity, κ is a epicyclic frequency, ν is a vertical frequency, The first term on the right-hand side in equation (1) is the Coriolis force, the second term is a combination of centrifugal and tidal forces, and the third term is gravitational acceleration from other particles in the cluster. For the point-mass galaxy, $\kappa = \omega$. Also for the galaxy with flat rotation ($\rho \propto r^{-2}$), $\kappa = 2\omega$. In Table 1, the approximated relations between mass profile and κ/ω are summarized. The exact description will be given in section 2.

In this paper, we compare dynamical evolution of the star cluster in the tidal fields of patent galaxies with four different $\kappa^2/\omega^2 (= 1, 2, 2.5, 3)$, i.e. different mass profile. Throughout the paper, we set the initial tidal radii identically among clusters with different κ/ω. The tidal radius and that at the initial time are, respectively, expressed as

$$r_{\rm t} = \left(\frac{GM}{4\omega^2 - \kappa^2} \right)^{1/3}, \tag{2}$$

and

$$r_{\rm t,i} = (GM_{\rm i}/(4\omega^2 - \kappa^2))^{1/3}, \tag{3}$$

where G is the gravitational constant, M and $M_{\rm i}$ are the cluster mass and that at the initial time. In the condition, the Coriolis force is relatively stronger for larger κ^2/ω^2, i.e. shallower mass profile. Although several studies set parent galaxy to have mass density profile other than point mass (Portegies Zwart et al. 2001a; Portegies Zwart et al. 2002; Portegies Zwart et al. 2003; Moore 1996; Baumgardt and Makino 2003; Portegies Zwart et al. 2001b; Yim and Lee 2002; Dehnen et al. 2004; Capuzzo Dolcetta et al. 2005; Combes et al. 1999), they aim to study disruption of star clusters taking place in relatively short timescale. On contrary to them, we investigate systematically the effects of the difference of mass density profile of parent galaxy on long-term mass-loss timescale of clusters .

The plan of this paper is as follows. In section 2, we give an exact description on the equation of motion in the tidal field. In section 3, we first perform orbital calculation in the fixed potential of star clusters and we compare the escape time delays of the potential escapers, which complicates the scaling with two-body relaxation timescale. In section 4, we perform N-body simulation of clusters in the tidal field in order to study the influence of mass density profiles of the parent galaxy on the mass-loss timescale of the star clusters. In section 5, we apply our simulation results for galactic globular clusters. Finally we summarize our paper in section 6.

2. Equation of Motion

In this section, we derive the equation of motion of stars in a cluster which moves circularly around a spherically symmetric parent galaxy with various mass density profiles. We set coordinate system which moves with the cluster. The origin of the coordinate system is set at the cluster center, the x axis is oriented in the opposite direction of the galactic center, and the z axis is along with the angular velocity vector of the cluster. Then, irrespective of the mass density profile of parent galaxy, we express the equation of motion of the cluster stars as

$$\frac{d^2\mathbf{r}_i}{dt^2} = -2\boldsymbol{\Omega} \times \frac{d\mathbf{r}_i}{dt} - \boldsymbol{\Omega} \times \left\{ \boldsymbol{\Omega} \times \left[\mathbf{r}_i + \begin{pmatrix} R_g \\ 0 \\ 0 \end{pmatrix} \right] \right\} - \nabla\Phi_{G,i} - \nabla\Phi_{c,i}, \tag{4}$$

where $\mathbf{r}_i$ is the position vector of i-th star, $\boldsymbol{\Omega}$ is the angular velocity vector of the cluster, R_g is the distance between the galactic center and the cluster center, and $\Phi_{G,i}$ and $\Phi_{c,i}$ are, respectively, the potential of the parent galaxy and the cluster at the position of the i-th star. The first and second terms in equation (4) are, respectively, the Coriolis and centrifugal forces on the i-th star.

We consider the situation where the size of the cluster is sufficiently smaller than the distance from the galactic center to the cluster. Then, the galactic potential Φ_G can be expanded in Taylor series around the cluster center, such as

$$\Phi_G \simeq \Phi_G|_{\mathbf{0}} + \frac{\partial\Phi_G}{\partial x}\bigg|_{\mathbf{0}} x + \frac{1}{2}\frac{\partial^2\Phi_G}{\partial x^2}\bigg|_{\mathbf{0}} x^2 + \frac{1}{2}\frac{\partial^2\Phi_G}{\partial y^2}\bigg|_{\mathbf{0}} y^2 + \frac{1}{2}\frac{\partial^2\Phi_G}{\partial z^2}\bigg|_{\mathbf{0}} z^2, \tag{5}$$

where $\mathbf{0} = (0,0,0)$ is the zero vector, the subscripts of $\mathbf{0}$ indicate the galactic potential and its derivatives at $\mathbf{0}$. Since the galactic potential is spherically symmetric, $(\partial\Phi_G/\partial y)_{\mathbf{0}} = (\partial\Phi_G/\partial z)_{\mathbf{0}} = 0$. Furthermore, $(\partial\Phi_G/\partial x)_{\mathbf{0}} = R_g\omega^2$, and $(\partial^2\Phi_G/\partial y^2)_{\mathbf{0}} = (\partial^2\Phi_G/\partial z^2)_{\mathbf{0}} = \omega^2$, where ω is the angular speed of the cluster around the galactic center, i.e. $\boldsymbol{\Omega} = (0,0,\omega)$. Finally, equation (5) is rewritten as

$$\Phi_G \simeq \Phi_G|_{\mathbf{0}} + R_g\omega^2 x + \frac{1}{2}\frac{\partial^2\Phi_G}{\partial x^2}\bigg|_{\mathbf{0}} x^2 + \frac{1}{2}\omega^2 y^2 + \frac{1}{2}\omega^2 z^2. \tag{6}$$

Substituting equation (6) into equation (4), the equation of motion of the i-th star is expressed as

$$\frac{d^2\mathbf{r}_i}{dt^2} = -2\boldsymbol{\Omega} \times \frac{d\mathbf{r}_i}{dt} - \begin{pmatrix} (\kappa^2 - 4\omega^2)x_i \\ 0 \\ \omega^2 z_i \end{pmatrix} - \nabla\Phi_{c,i}, \tag{7}$$

where

$$\kappa^2 = \frac{\partial^2\Phi_G}{\partial x^2}\bigg|_{\mathbf{0}} + 3\omega^2, \tag{8}$$

and κ is so-called epicyclic frequency.

The epicyclic frequency, κ, and angular speed of the cluster, ω, are determined by the mass density profile of the galaxy, ρ_G, and the distance between the galactic center and the cluster center, R_G. The angular speed, ω, is expressed as

$$\omega^2 = \frac{GM_g(0)}{R_g^3} = \frac{4}{3}\pi G\overline{\rho_G}(0), \tag{9}$$

where $M_g(0)$ and $\overline{\rho_G}(0)$ are, respectively, the galactic mass and average mass density within the galactic radius, R_g. Since the mass density profile is spherically symmetric, the galactic potential, Φ_G, is expressed as

$$\Phi_G = -4\pi G\left[\frac{1}{x+R_g}\int_{-R_g}^{x}\rho_G(x')(x'+R_g)^2\,dx' + \int_{x}^{\infty}\rho_G(x')(x'+R_g)\,dx'\right]. \tag{10}$$

Differentiating partially equation (10) with respect to x, we obtain

$$\frac{\partial^2 \Phi_{\mathrm{G}}}{\partial x^2} = -\frac{2GM_{\mathrm{g}}(x)}{(x+R_{\mathrm{g}})^3} + 4\pi G\rho_{\mathrm{G}}(x), \tag{11}$$

and therefore,

$$\left.\frac{\partial^2 \Phi_{\mathrm{G}}}{\partial x^2}\right|_{\mathbf{0}} = -2\omega^2 + 4\pi G\rho_{\mathrm{G}}(0). \tag{12}$$

Substituting equation (12) into equation (8), we obtain the ratio of the epicyclic frequency to the angular speed, such as

$$\frac{\kappa^2}{\omega^2} = 1 + \frac{4\pi G\rho_{\mathrm{G}}(0)}{\omega^2} = 1 + 3\frac{\rho_{\mathrm{G}}(0)}{\overline{\rho_{\mathrm{G}}}(0)}, \tag{13}$$

where the second equality in equation (13) comes from equation (9).

From equation (13), we can confirm the relation between the mass density profile of the galaxy and the ratio of κ^2 to ω^2 in table 1. Since $\rho_{\mathrm{G}}(x) = 0$ in the case of $\rho_{\mathrm{G}}(x) \propto R^{-\infty}$, we can see immediately $\kappa^2 = \omega^2$. We consider the case:

$$\rho_{\mathrm{G}}(x) = C(x+R_g)^{-k} \ (0 \leq k \leq 2). \tag{14}$$

Therefore, the average mass density within the galactic radius, R_{g}, is expressed as

$$\overline{\rho_{\mathrm{G}}}(0) = \frac{\int_{-R_{\mathrm{g}}}^{0} 4\pi(x+R_{\mathrm{g}})^2 \rho_{\mathrm{G}} dx}{4\pi R_{\mathrm{g}}^3/3} = \frac{3}{3-k}C(x+R_{\mathrm{g}})^{-k}, \tag{15}$$

where the second equality is obtained by using equation (14). Substituting equation (14) and (15 into equation (13), equation (13) is rewritten as

$$\frac{\kappa^2}{\omega^2} = 4 - k \ (0 \leq k \leq 2). \tag{16}$$

The tidal radius is defined as the distance from the cluster center to a Lagrange point, and can be expressed by equation (2). In this paper, we investigate the cluster evolution by parameterizing the mass density profile of the galaxy, ρ_{G}, and the initial tidal radius given by equation (3), not the mass density profile of the galaxy, ρ_{G}, and the distance between the galactic center and the cluster center, R_{g}. We regard the initial tidal radius, $r_{\mathrm{t,i}}$ as one of the most important parameter for the mass-loss timescale of the cluster, since in paper I we found that the longer the mass-loss timescale of the cluster becomes, the larger the initial tidal radius is even if the mass density profile of the galaxy is equal.

We consider the situation where the initial tidal radius, $r_{\mathrm{t,i}}$, i.e. $(4\omega^2 - \kappa^2)$, is kept constant. From equation (13), the angular speed, ω, becomes larger, as the mass density profile of the galaxy becomes shallower, or $\rho_{\mathrm{G}}(0)/\overline{\rho_{\mathrm{G}}}(0)$ becomes smaller. In the equation of motion (7), the Coriolis force becomes larger as the mass density profile of the galaxy becomes shallower.

As an example, we investigate the difference of the Coriolis forces between point-mass galaxy ($\rho_{\mathrm{G}}(x) = 0, x > -R_{\mathrm{G}}$) and isothermal sphere galaxy ($\rho_{\mathrm{G}}(x) = 3M_{\mathrm{G}}(0)/(4\pi R_{\mathrm{G}}(x+R_{\mathrm{G}})^2), x > -R_{\mathrm{G}}$). The values of κ^2/ω^2 in point-mass galaxy and isothermal sphere galaxy are 1 and 2, respectively. Then, Coriolis force increases by 20 % from the case of point-mass galaxy to that of isothermal sphere galaxy. The Coriolis force changes angular momentum of cluster stars around cluster center. The difference of the Coriolis force may affect escape of cluster stars.

3. Orbital Calculation of Potential Escaper in Fixed Potential

In this section, we perform orbit calculations in the fixed and smooth cluster potential in order to investigate the escape time delay of the potential escapers. Due to their mutual encounters, stars gain enough energy to escape from the clusters and become the potential escaper. Such process takes place in two-body relaxation timescale. In the tidal field, the potential escapers can escape only through small apertures around the two Lagrangian points, and can remain inside the clusters before the escape on timescale comparable to two-body relaxation time (FH). Therefore, such escape time delay can influence on the escape timescale or the mass-loss timescale of the star clusters.

3.1. Method

We calculate the orbits of the potential escapers in a fixed and smoothed potential due to cluster stars plus the steady tidal field of the parent galaxy. The equation of motion of the potential escapers is described in equation (7). For the cluster potential, $\Phi_{\mathrm{c},i}$, we use $W_0 = 3$ King model, where W_0 indicates initial dimensionless central potential. In order to compute the acceleration from the King model, $\nabla\Phi_{\mathrm{c},i}$, in equation (7), we use cubic spline interpolation between grid data obtained by a numerical solution (e.g. Press et al. 1992).

Regardless of the mass density profile of the parent galaxy, we set the initial tidal radius of the cluster, $r_{t,i}$ to be equal to the radius beyond which the density is zero in the $W_0 = 3$ King model, denoted by r_{kg}. The value of r_{kg} is 3.13, where we use standard units (Heggie, Mathieu 1986), such that $M_i = G = -4E_c = 1$, where E_c is the initial total energy within the cluster. When $r_{t,i} = r_{kg} = 3.13$, the values of κ and ω are determined for each given ratio κ^2/ω^2, using equation (13) and (2). We performed the orbital calculations for 4 models in which the parent galaxy has mass density profiles of $\kappa^2/\omega^2 = 1, 2, 2.5, 3$. The values of κ^2 and ω^2 are showed in table 2. The second right column shows representative mass density profiles of the parent galaxy in each ratio of κ^2/ω^2, such as single power law models.

We determine the escape time delay as the duration between $t = 0$ and the time when escape condition, $|x_i| > r_t$, is satisfied. Note that the tidal radius, r_t, remains the initial tidal radius, $r_{t,i}$, during the calculation, since clusters do not lose the mass in this calculations.

We calculate sets of orbits of the potential escapers for several values of relative energy excess, $\hat{E}_{pot,i} = (E_{pot,i} - E_{crit})/|E_{crit}|$, where $E_{pot,i}$ is the energy of i-th potential escaper, given by

$$E_{pot,i}(t) = \frac{1}{2}(v_{xi}^2 + v_{yi}^2 + v_{zi}^2) + \Phi_{c,i} - \frac{1}{2}(\kappa^2 - 4\omega^2)x_i^2 + \frac{1}{2}\omega^2 z_i^2, \qquad (17)$$

where v_{xi}, v_{yi}, and v_{zi} are x, y, and z components of the velocity of i-th particle, respectively.

We integrate the orbits of the stars by means of adaptive stepsize control for a forth-order Runge-Kutta method (e.g. Press et al. 1992). The integration error in energy is about 9×10^{-5} at maximum ($\hat{E}_{pot,i} = 0.03$ at $t = 3 \times 10^7$ in standard units in the shallowest mass density profile of parent galaxy, $\kappa^2/\omega^2 = 3$).

3.2. Results

In this subsection, we present the results of the orbital calculations of the potential escapers. In section 3.2.1, we investigate the difference of orbit families in planar orbits ($z = 0$ plane) among parent galaxies with different mass density profiles. As the profile of the parent galaxy is shallower, more potential escapers move in regular-like orbit, and have larger escape time delay. In section 3.2.2, we show that this is also applicable to non-planar orbit families. In section 3.2.3, we investigate the distribution of the escape time delay in order to see whether the difference of orbit families affects the escape rate of potential escapers.

3.2.1. Orbital families in planar orbits

At first, our investigation is confined to the orbits of potential escapers on $z = 0$ plane for simplicity of the analyses. If we give the potential escapers initial conditions where $z_i = 0$ and $\dot{z}_i = 0$, their orbits are confined to $z = 0$ plane forever shown in equation (7).

In figure 1, we illustrate orbits and surfaces of section for 10 potential escapers with various escape time, t_e, for each model of $\kappa^2/\omega^2 = 1, 2, 2, 5, 3$. We plot the orbit until the escape or $t = 500$ for non-escaper, and the surfaces of section until the escape or $t = 10^6$ for non-escaper. Here and hereafter, potential escapers which are still in clusters when orbit calculations are terminated are called "non-escaper". We define the surface of section as $(x, \dot{x})$ at which the potential escapers cross x axis in the direction of $\dot{y} > 0$.

At initial, we distribute 1000 potential escapers of $\hat{E}_{pot,i} = 0.03$ uniformly in $(x, y, \dot{x}, \dot{y})$ phase space, and calculate the escape time delays. We sort the 1000 potential escapers in small order of the escape time delay. We chose k-th potential escapers, where $k = 50 + 100(i-1)(i = 1, 2, \ldots, 10)$ (hereafter, we call $k(i)$-th potential escapers "i-th potential escapers"), and show the orbit and surface of section of i-th potential escaper in i-th panel of each model in figure 1 from left to right. As for the non-escapers, the selection are done at random.

In the models of two steeper mass density profiles ($\kappa^2/\omega^2 = 1$ and 2), the orbits become regular-like gradually from left to right. In both models, the $7 - 10$th potential escapers looks like regular. However, in the models of two shallower mass density profile galaxies ($\kappa^2/\omega^2 = 2.5$ and 3), the orbits are seen to become regular-like suddenly at the 5th potential escapers.

In all models, there are potential escapers whose surfaces of section are confined to small phase space, and they correspond to non-escapers. We call these orbits "regular orbits". In the model of the shallow mass density profile ($\kappa^2/\omega^2 = 2.5$), some orbits seem regular, but their surfaces of section occupy larger space than regular orbits, and eventually escape from the clusters, such as 6th and 7th potential escapers. We call these orbits "semi-regular orbits".

We consider the difference among the regular, semi-regular, and the other orbits. In figure 2 we put together surface of section of the 1st, 2nd, …, 10th potential escapers in each model. The colors and shapes in surface of section are divided according to non-regular (white triangles), semi-regular (white or gray squares), and regular orbits (black circles), where we define semi-regular orbit as the orbit of potential escapers which have escape time delay, $t_e > 100$ and non-regular orbit as escape time delay, $t_e < 100$. The surfaces of section of semi-regular orbits, whose escape time delay is $t_e > 100$, are divided into two colors, white and gray. The difference of the colors shows not the difference among the potential escapers, but that of the time when the potential escapers cross x axis in the direction of $\dot{y} > 0$. If the potential escapers cross x axis in the direction of $\dot{y} > 0$ less and more than 100 time units before they escape from the cluster, the colors of the surfaces of section are, respectively, white and gray.

The region in the surface of section occupied by the non-regular and semi-regular orbits is different from that of regular orbits in each model. The region in the surface of section for non-regular orbits is similar to that of semi-regular orbits just before escape, i.e. that of gray squares, and different from that of semi-regular orbits not just before escape, i.e. that of white squares. From the above, we guess that the escape time delay of any potential escaper depends on their initial phase space.

Figure 3 shows the escape time delay of potential escapers against the initial phase space $(x, \dot{x})$. The uppermost 4 panels show the potential escapers whose initial phase is $y = 0$, $z = 0$, $\dot{y} > 0$, and $\dot{z} = 0$. The points are colored according to the escape time delay, t_e, of the potential escapers. Black regions show non-escapers, and the lightest regions show the potential escapers of $t_e < 10^2$. The escape time delay depends on the initial phase of the potential escapers. As the mass density profile of the parent galaxy is shallower from $\kappa^2/\omega^2 = 1, 2$ to $\kappa^2/\omega^2 = 2.5$, the phase volume for $10^2 < t_e < 10^4$ becomes smaller, and that of $t_e > 10^4$ becomes larger. Furthermore, as the mass density profile of the parent galaxy becomes shallower from $\kappa^2/\omega^2 = 2.5$ to 3, the phase space for $10^4 < t_e < 10^6$ is replaced by that of non-escapers. The phase space of $t_e < 10^2$ is similar in all models.

In summary, we find that there is a larger fraction of regular-like orbital families in the parent galaxy with shallower mass density profiles. The difference in the orbital families among galaxy models brings the structure in initial phase space about their escape time delay shown in uppermost panel of figure 3.

3.2.2.   Orbital families in non-planar orbits

Figure 3 shows the escape time delay against the initial phase $(x, \dot{x})$ also for non-planar orbits. The points are colored according to the escape time delay of potential escapers. In each panels the escape time delay of the potential escapers whose initial positions and velocities of z-component are in limited ranges are only plotted, and whose initial positions and velocities of y-component are $y = 0$, and $\dot{y} > 0$. The z components increase from top panels to bottom panels. The structure in initial phase against the escape time delay seen in z=0 planer orbit can be also seen in other non-planer orbit, though the structure becomes less fine as the z components increases.

3.2.3.   Distribution of escape time delay

Figure 4 shows fractions, F_{pot}, of potential escapers which do not escape at a given time t. The curves are drawn, from left to right, in order of large initial relative energy excess, $\hat{E}_{pot,i} = 0.24, 0.16, 0.12, 0.08, 0.06, 0.04$ and 0.03. We spatially distribute them in the same way as primordial population in $W_0 = 3$ King model immersed in a tidal field of parent galaxy. The vertical lines at the right side show the times when the integrations are terminated. A common feature in all models is that the potential escapers of larger relative energy excess, $\hat{E}_{pot,i}$, have smaller escape time delay and smaller fraction of non-escapers. The feature in the case of the point mass ($\kappa^2/\omega^2 = 1$) agrees with the result of FH.

Figure 5 shows the fractions, F_{pot}, of potential escapers which do not escape at a given time t. We plot together the fractions, F_{pot}, of all models of κ^2/ω^2 in each relative energy excess, $\hat{E}_{pot,i} = 0.03, 0.08$ and 0.24. The potential escapers in parent galaxy with shallower mass density profile escape more slowly, which agrees with the difference of orbit families described in section 3.2.1.

We try to explain the difference of escape time delay among different $\hat{E}_{pot,i}$ and κ^2/ω^2 based on phase space flux of orbits of potential escapers. We define phase space flux near Lagrange points as amount of phase space which flows near Lagrange points in the outward direction with respect to the cluster per time unit. If potential escapers are equally present in every phase space, the number of escapers from the cluster should be proportional to the above phase space flux. In FH, which is the same as model of $\kappa^2/\omega^2 = 1$, the phase space flux may explain the dependence of escape time delay on relative energy excess.

The phase space flux, $\mathcal{F}$, per unit energy is expressed (MacKay 1990) by

$$\mathcal{F} = 2 \int_{\dot{x}' > 0} \delta \left[\phi' + \frac{1}{2}(\dot{x}'^2 + \dot{y}'^2 + \dot{z}'^2) - E \right] \dot{x}' d\dot{x}' d\dot{y}' d\dot{z}' dy' dz', \tag{18}$$

where $x', y', z', \dot{x}', \dot{y}'$, and $\dot{z}'$ are coordinate and velocity when the origin is located in a Lagrange point which have $x = r_t$, and ϕ' is obtained by expanding the effective potential, ϕ, around the Lagrange point to second order. ϕ and ϕ' is respectively expressed by

$$\phi = -\frac{1}{2}(\kappa^2 - 4\omega^2)x^2 + \frac{1}{2}\omega^2 z^2 + \Phi_c, \tag{19}$$

where $\Phi_c = -GM/r_t$, and

$$\phi' - E_{crit} = \frac{3}{2}(\kappa^2 - 4\omega^2)x'^2 - \frac{1}{2}(\kappa^2 - 4\omega^2)y'^2 - \frac{1}{2}(\kappa^2 - 5\omega^2)z'^2. \tag{20}$$

Since there are two Lagrange points, we must add coefficient of 2 to integral. In equation (18), ϕ' is evaluated at $x' = 0$. We integrate equation (18), and obtain

$$\mathcal{F} = \frac{4\pi^2 (E - E_{\mathrm{crit}})^2}{\sqrt{(4\omega^2 - \kappa^2)(5\omega^2 - \kappa^2)}}. \tag{21}$$

A familiar calculation shows that the phase space volume per unit energy is expressed by

$$\mathcal{V} = 4\pi \int \sqrt{2(E - \phi)} d^3 \mathbf{r}, \tag{22}$$

where the integration is done over the inside cluster. This does not depend sensitively on E in the vicinity of $E = E_{\mathrm{crit}}$, and so we evaluate it by a Monte Carlo technique. The phase space fluxes and volumes per energy in $\hat{E}_{\mathrm{pot}} = 0.03$ and the timescale of phase space flux, $t_{\mathrm{ph}} = \mathcal{V}/\mathcal{F}$, are summarized in table 3.

Figure 6 shows the fraction, F_{esc}, of escapers which do not escape at a given time scaled by the timescale of the phase space flux, t/t_{ph}. We exclude non-escapers from figure 4. As seen in figure 6, the F_{esc} curves are in good agreement in three steeper mass density profiles ($\kappa^2/\omega^2 = 1, 2, 2.5$). The result in the case of point-mass galaxy agrees with that of FH. We can see that escape time delay, t_{e}, is proportional to the timescale of the phase space flux, $t_{\mathrm{ph}} \propto (E - E_{\mathrm{crit}})^{-2} \propto \hat{E}^{-2}$ in the case of steeper mass density profile of parent galaxy ($\kappa^2/\omega^2 \leq 2.5$). However, in the shallowest mass density profile ($\kappa^2/\omega^2 = 3$), the agreement becomes worse.

In Figure 7, the fraction, F_{esc} of $\hat{E}_{\mathrm{pot},i} = 0.03$ for all models are plotted together against time scaled by the timescale of the phase space flux, t/t_{ph}. Agreement in the curves is not good, and escape time delay scaled by the timescale of the phase space flux, $t_{\mathrm{e}}/t_{\mathrm{ph}}$, are longer as the mass density profile of the parent galaxy becomes shallower. Figure 7 shows that the timescale of the phase space flux may not well explain the dependence of the escape time delay the on mass density profile of the parent galaxy.

4. *N*-body Simulations

In this section, we present results of N-body simulations of star clusters, and investigate how the dependence of escape time delay on mass density profile of parent galaxy influence the mass-loss timescale of clusters. In section 4.1, we describe the simulation method. In section 4.2, we show the results, and find that mass-loss timescale becomes larger as mass density profile of parent galaxy is shallower.

4.1. Simulation method

We investigate mass loss of star clusters in an external tidal field by means of N-body simulations. The equation of motion is described in equation (7). In our simulations we use a softened gravitational potential, and the third term of equation (7) is expressed as

$$-\nabla \Phi_{\mathrm{c},i} = - \sum_{j=1, j\neq i}^{N} \frac{G m_j (\mathbf{r}_i - \mathbf{r}_j)}{\left(|\mathbf{r}_i - \mathbf{r}_j|^2 + \varepsilon^2\right)^{3/2}}, \tag{23}$$

where m_j is mass of j-th particle and ε is a softening parameter. We set the softening parameter, ε, as $1/32$, where we use the standard units, $M_{\mathrm{i}} = G = -4 E_{\mathrm{c}} = 1$, as section 2.

We use $W_0 = 3$ King's models (King 1966) to generate initial distribution of star clusters. We perform eight sets of simulations of star clusters with different initial tidal radii, $r_{\mathrm{t},i}$, and different mass density profiles of parent galaxies, κ^2/ω^2, as summarized in table 2. The number of particles used for runs are $N = 2^i$ in the range described in table 2. All particles have the same mass, $m = M_{\mathrm{i}}/N$. We perform five runs whose realization of particle distribution are different for each N when $N \leq 8192$, and one run when $N \geq 16384$, except for model $r_{\mathrm{t},i}/r_{\mathrm{kg}} = 2.2$ and $\kappa^2/\omega^2 = 3$. For this model, five runs when $N \leq 4096$, and one run when $N \geq 8192$.

The simulation code is the same as that used in Paper I. We perform numerical integrations of equation (1) using a leap-frog integration scheme with shared and constant timestep. The stepsize, Δt, is set to be as $1/64$ in models $r_{\mathrm{t},i}/r_{\mathrm{kg}} = 1.0$ and $\kappa^2/\omega^2 = 1, 2, 2.5$, and as $1/128$ in the other models. We used the Barnes-Hut tree algorithm (Barnes, Hut 1986) on GRAPE-5 (Kawai et al. 2000), a special-purpose computer designed to accelerate N-body simulations. We use only the dipole expansion and the opening parameter $\theta = 0.5$. It spend about 500 CPU hours completing the longest run, $N = 32768$ in models which have larger tidal radii ($r_{\mathrm{t},i}/r_{\mathrm{kg}} = 2.2$) and the steepest mass density profile of parent galaxy ($\kappa^2/\omega^2 = 1$). For smaller N simulations, the force calculation is done by direct summations (when $N \leqq 4096$) and on host computer (without GRAPE-5, when $N \leqq 512$).

Contrary to the standard star cluster simulations, our simulation uses a softened gravitational potential and a leap-flog integrator with a relatively large stepsize. Also, the force calculation is performed with the tree algorithm. We adopt these approaches, since we partly use mass-loss timescale obtained in paper I, which modeled mass density profile as the point-mass one ($\kappa^2/\omega^2 = 1$). As discussed in paper I, the approaches that we adopt do not influence the results concerning escape from the cluster.

4.2. Results

Figure 8 shows evolutions of the total mass for all models. The curves indicate the decrease in mass of the cluster defined by a tidal boundary. We define geometrically the cluster member as all stars within the tidal radius from the center of mass of the cluster, which is expressed as equation (2). Since M depends on r_t, itself, some iteration is usually required. We remove stars when they escape far enough (more than 4096 length units from the coordinate origin).

Figure 9 shows the mass-loss timescale of the clusters as a function of the initial half-mass relaxation time, $t_{rh,i}$ in the upper panels. The lower panels show the mass-loss timescale of the clusters scaled by those in the parent galaxy with the steepest mass density profile ($\kappa^2/\omega^2 = 1$). The mass-loss timescale is here defined as the time when 50% of the initial total mass is lost. Since we perform several runs for each model, we use the means of these runs as the mass-loss timescale, t_{mloss}. Table 4 gives the maximum deviations from the means among these runs. Since we use the potential softening and fix the softening parameters for all models, the initial half-mass relaxation time, $t_{rh,i}$, is expressed as

$$t_{rh,i} = 0.138 \frac{N r_{h,i}^{3/2}}{M_i^{1/2} G^{1/2} \ln(0.079 r_{h,i}/\varepsilon)}, \tag{24}$$

where $r_{h,i}$ is the initial half-mass radius. The Coulomb logarithm, Λ, is expressed as the ratio p_{max}/p_{min}, where p_{max} and p_{min} are, respectively, the maximum and minimum impact parameters. Since the maximum impact parameter, p_{max}, is about the system size, it is expressed as $p_{max} = a r_{h,i}$. The minimum impact parameter, p_{min}, is determined by the softening parameter, ε. Therefore, $p_{min} = b\varepsilon$. A ratio of $a/b = 0.079$ is taken so that the evolutions of the minimum potential in a cluster would have no difference between runs for three different softening parameters, ε, as can be seen in the lower panel of figure 15 of paper I. Thus, the initial half-mass relaxation timescale, $t_{rh,i}$, was estimated as $t_{rh,i} = 1200 \times (N/8192)$. The initial half-mass radii in the standard unit are $r_{h,i} = 0.84$.

Even if clusters have the same initial half-mass relaxation time, the clusters lose their mass more slowly in the parent galaxy with shallower profile. For models in a moderately strong tidal field ($r_{t,i}/r_{kg} = 1.0$), clusters in parent galaxy with shallower mass density profile ($\kappa^2/\omega^2 = 2, 2.5, 3$) have larger mass-loss timescale than those in the parent galaxy with the steepest mass density profile ($\kappa^2/\omega^2 = 1$) by 20 %, 50 %, and factor of 2.5 respectively. On the other hand, the largest difference of mass-loss timescale is at most 60 % for the case in weak tidal field ($r_{t,i}/r_{kg} = 2.2$). As the tidal field becomes stronger, sensitivity of mass-loss timescale to mass density profile of parent galaxy is enhanced.

We consider possibilities other than escape time delay for the difference of mass-loss timescale among clusters in different parent galaxy. At first, we check whether the difference of mass-loss timescale is affected by tidal lock. Since clusters set so far rotate around itself at angular velocity $(0, 0, \omega)$ with respect to inertia frame, their rotation speeds around itself are different among clusters in parent galaxy with different mass density profiles.

We perform N-body simulations of clusters which rotate solidly at angular vector $(0, 0, -\omega)$ in the same reference frame described in section 2. The clusters have $W_0 = 3$ King profile and are in a moderate tidal radius, $r_{t,i}/r_{kg} = 1.0$. These clusters do not rotate with respect to inertia frame. Figure 10 shows mass-loss timescale of clusters tidally unlocked, and mass-loss timescale scaled by mass-loss timescale of clusters tidally unlocked in the parent galaxy with the steepest mass density profile ($\kappa^2/\omega^2 = 1$).

Mass-loss timescale and the increase from steeper mass density profile of parent galaxy to shallower one are not distinguishable among clusters tidally locked and unlocked. Therefore, tidal lock is not responsible for the difference of mass-loss timescale among clusters in parent galaxy with different mass density profile.

Next, we check whether two-body relaxation, which induces the escape of stars, is influenced by the difference of mass density profile of parent galaxy. However, we find that two-body relaxation does not change. Figure 11 shows the change in energy of an individual star for clusters in parent galaxy with mass density profile $\kappa^2/\omega^2 = 1, 2, 2.5, 3$, where $r_{t,i}/r_{kg} = 1.0$, and the clusters have $N = 1024$. In figure 11 we plot $\{E_{max,i}\}_{med}$, the median value of the maximum energy records at a given time, t_1:

$$E_{max,i}(t_1) = \max_{t < t_1}\{E_i(t)\}, \tag{25}$$

$$E_i(t) = \frac{1}{2}(v_{xi}^2 + v_{yi}^2 + v_{zi}^2) + \Phi_{c,i} - \frac{1}{2}(\kappa^2 - 4\omega^2)x_i^2 + \frac{1}{2}z_i^2, \tag{26}$$

of 50 randomly selected particles. We did not update $E_{max,i}(t_1)$ after stars escaped from the cluster. The representative value, $\{E_{max,i}\}_{med}$, may trace the energy acquired by two-body relaxations, on the average. When stars obtain enough energy, they escape from cluster eventually. The dashed lines indicate the escape energy of each model, which is potential at Lagrange points and expressed by

$$E_{crit} = -\frac{3GM}{2r_t}. \tag{27}$$

As shown in figure 11, steep increase of $\{E_{\max,i}\}_{\mathrm{med}}$ from -0.8 to -0.6 are similar among all clusters. The increases of $\{E_{\max,i}\}_{\mathrm{med}}$ at $t < 400$ are very similar among parent galaxy with steeper mass density profile ($\kappa^2/\omega^2 = 1, 2, 2.5$). The facts above indicates that the relaxation processes in all models occur on almost the same timescale. The deviation of the shallowest model ($\kappa^2/\omega^2 = 3$) from other models after $t = 100$ is due to the much slower mass loss than those of other clusters.

5. Evaluation Formula and Implication for Observed Galactic Globular Clusters

In this section, we formulate mass-loss timescale of globular clusters, using our simulation results. From the formula, we obtain properties of globular clusters which survive over the Hubble time. We compare the properties with those of the observed galactic globular clusters, and examine the validity of our formula for the mass-loss timescale.

5.1. A formula of mass-loss timescale

We derive an evaluation formula for the mass-loss timescale of a globular cluster using the result of Paper I and this paper that the mass loss timescale is proportional to the half-mass relaxation time, $t_{\mathrm{mloss}} \propto t_{\mathrm{rh}}^x$, and a correction factor for the difference of the mass-loss timescale among mass profiles of parent galaxies. We write the mass-loss timescale of a globular cluster, t_{mloss}, as

$$t_{\mathrm{mloss}}(\tilde{r}_{\mathrm{t}}, \kappa^2/\omega^2) = t_{\mathrm{mloss}, t_{\mathrm{rh}}=t_0}(\tilde{r}_{\mathrm{t}}) \left(\frac{t_{\mathrm{rh,i}}}{t_0}\right)^{x(\tilde{r}_{\mathrm{t}})} \left[1 + f(\kappa^2/\omega^2) g(\tilde{r}_{\mathrm{t}})\right]., \tag{28}$$

where

$$\tilde{r}_{\mathrm{t}} \equiv r_{\mathrm{t,i}}/r_{\mathrm{h,i}}. \tag{29}$$

The product of the first and second factors in the right-hand side of equation (28) represents the mass-loss timescale of a cluster in a tidal field produced by a point-mass galaxy. The timescale $t_{\mathrm{mloss}, t_{\mathrm{rh}}=t_0}(\tilde{r}_{\mathrm{t}})$ is mass-loss timescale of a cluster whose initial half-mass relaxation time $t_{\mathrm{rh,i}}$ is a given time t_0. The third factor in the right-hand side of equation (28) represents the increment from mass-loss timescale of clusters in a point-mass galaxy to those with shallower galaxy.

We construct fitting formulae for four functions in equation (28), $t_{\mathrm{mloss}, t_{\mathrm{rh}}=t_0}(\tilde{r}_{\mathrm{t}})$, $x(\tilde{r}_{\mathrm{t}})$, $g(\tilde{r}_{\mathrm{t}})$, and $f(\kappa^2/\omega^2)$, using our simulation results summarized in table 5. For the function $t_{\mathrm{mloss}, t_{\mathrm{rh}}=t_0}(\tilde{r}_{\mathrm{t}})$, we use those of clusters whose initial half-mass relaxation time is 1000 N-body time unit, $t_{1000}(\tilde{r}_{\mathrm{t}}) \equiv t_{\mathrm{mloss}, t_{\mathrm{rh}}=1000 t_{\mathrm{nu}}}(\tilde{r}_{\mathrm{t}})/t_{\mathrm{nu}}$, where t_{nu} is the N-body time unit. The simulation results of the mass-loss timescale $t_{1000}(\tilde{r}_{\mathrm{t}})$ are shown in the third column of table 5. The fitting formula of $t_{1000}(\tilde{r}_{\mathrm{t}})$ is given as

$$t_{1000}(\tilde{r}_{\mathrm{t}}) \approx t_{1000,\mathrm{fit}}(\tilde{r}_{\mathrm{t}}) = 2 \times 10^4 \frac{\tilde{r}_{\mathrm{t}}^4}{\tilde{r}_{\mathrm{t}}^4 + 2 \times 10^3}. \tag{30}$$

As seen in the upper panel of figure 12, equation (30) is well fit to the mass-loss timescale, $t_{1000}(\tilde{r}_{\mathrm{t}})$, over an intermediate range of $\tilde{r}_{\mathrm{t}} = 3$ - 20. Since a cluster immediately loses its mass in the strong limit of a tidal field, $t_{1000}(\tilde{r}_{\mathrm{t}}) \to 0$ in the limit of $\tilde{r}_{\mathrm{t}} \to 0$. Since mass-loss timescale of a cluster does not depend on the strength of the tidal field in the weak limit, $t_{1000}(\tilde{r}_{\mathrm{t}})$ should asymptotically approach to a constant value.

For the function $x(\tilde{r}_{\mathrm{t}})$, we use those at the initial half-mass relaxation time $t_{\mathrm{rh,i}}$ is $1000 t_{\mathrm{nu}}$, which is shown in the fourth column of table 5. The fitting formula of the function $x(\tilde{r}_{\mathrm{t}})$ is given as

$$x(\tilde{r}_{\mathrm{t}}) \approx x_{\mathrm{fit}}(\tilde{r}_{\mathrm{t}}) = \frac{\tilde{r}_{\mathrm{t}}^4}{\tilde{r}_{\mathrm{t}}^4 + 1 \times 10^2}. \tag{31}$$

As seen in the lower panel of figure 12, equation (31) is well fit to the logarithmic slope, $x(\tilde{r}_{\mathrm{t}})$, over an intermediate range of $\tilde{r}_{\mathrm{t}}$. Since mass-loss timescale of a cluster does not depend on its initial half-mass relaxation time in the strong limit of a tidal field, $x(\tilde{r}_{\mathrm{t}}) \to 0$ in the limit of $\tilde{r}_{\mathrm{t}} \to 0$. Since mass-loss timescale of a cluster should be proportional to its initial half-mass relaxation time in the weak limit of a tidal field, $x(\tilde{r}_{\mathrm{t}})$ asymptotically approaches to unity.

We construct of the fitting formula for the increment from mass-loss timescale of a cluster in a point-mass galaxy to that in a shallower galaxy, $f(\kappa^2/\omega^2) g(\tilde{r}_{\mathrm{t}})$, as follows. We simplify the dependence of the increment on $\tilde{r}_{\mathrm{t}}$, such that the increment $f(\kappa^2/\omega^2) g(\tilde{r}_{\mathrm{t}})$ in a strong tidal field is the same as that for $\tilde{r}_{\mathrm{t}} = 3.9$, and the increment $f(\kappa^2/\omega^2) g(\tilde{r}_{\mathrm{t}})$ in a weak tidal field is zero. These are shown in the fifth column of table 5. The fitting formula of the function $f(\kappa^2/\omega^2)$ is given as

$$f\left(\kappa^2/\omega^2\right) \approx f_{\mathrm{fit}}\left(\kappa^2/\omega^2\right) = \frac{15}{16 - \left(\kappa^2/\omega^2\right)^2}, \tag{32}$$

and we adopt a step function for the fitting function of $g(\tilde{r}_{\mathrm{t}})$ as

$$g(\tilde{r}_{\rm t}) \approx g_{\rm fit}(\tilde{r}_{\rm t}) = \begin{cases} 1 & (\tilde{r}_{\rm t} \leq 8) \\ 0 & (\tilde{r}_{\rm t} > 8) \end{cases}. \tag{33}$$

As seen in figure 13, equation (32) is well fit to the increment obtained by our simulation of $\kappa^2/\omega^2 = 2, 2.5, 3$. The increment, $1 + f(\kappa^2/\omega^2)$, approaches to infinity at $\kappa^2/\omega^2 \to 4$.

5.2. Survivability of galactic globular clusters

Using equation (28), we obtain parameters of a cluster which survives over the Hubble time, 10^{10} years. We compare the parameters with those of the galactic globular clusters, and examine the validity of our formula for the mass-loss timescale. For obtaining the mass-loss timescale of a cluster from equation (28), the following set of parameters is required: the initial tidal radius, $r_{\rm t,i}$, the initial half-mass radius, $r_{\rm h,i}$, the initial half-mass relaxation time, $t_{\rm rh,i}$, and the mass profile of the parent galaxy, κ^2/ω^2.

Here we rewrite equation (28) using observable parameters of galactic globular clusters, the initial total mass of the cluster, $M_{\rm i}$, the average mass of the cluster stars, $\bar{m}$, the initial half-mass radius, $r_{\rm h,i}$, the mass profile of its parent galaxy, κ^2/ω^2, the circular velocity of the cluster, $v_{\rm c}$, and the distance of the cluster from the center of the parent galaxy, $R_{\rm G}$. Adopting $t_0 = 1000t_{\rm nu}$, equation (28) is rewritten as

$$t_{\rm mloss}(\tilde{r}_{\rm t}, \kappa^2/\omega^2) = t_{1000}(\tilde{r}_{\rm t})t_{\rm nu} \left(\frac{t_{\rm rh,i}}{1000t_{\rm nu}} \right)^{x(\tilde{r}_{\rm t})} \left[1 + f(\kappa^2/\omega^2)g(\tilde{r}_{\rm t}) \right]. \tag{34}$$

Substituting the four fitting formulae (30), (31), (32), and (33) into $t_{1000}(\tilde{r}_{\rm t})$, $x(\tilde{r}_{\rm t})$, $f(\kappa^2/\omega^2)$, and $g(\tilde{r}_{\rm t})$ in equation (34) respectively, we obtain an evaluation formula for the mass-loss timescale of clusters as

$$t_{\rm mloss}(\tilde{r}_{\rm t}, \kappa^2/\omega^2) \approx 1 \times 10^9 [\rm yr] \left[\frac{t_{1000,\rm fit}(\tilde{r}_{\rm t})}{t_{1000,\rm fit}(\tilde{r}_{\rm t} = 4)} \right] \left(\frac{r_{\rm h,i}}{3\rm pc} \right)^{3/2} \left(\frac{M_{\rm i}}{2 \times 10^4 M_\odot} \right)^{-1/2}$$

$$\times \left[\left(\frac{M_{\rm i}}{2 \times 10^4 M_\odot} \right) \left(\frac{\bar{m}}{0.3M_\odot} \right)^{-1} \right]^{x_{\rm fit}(\tilde{r}_{\rm t})} \left[1 + f_{\rm fit}(\kappa^2/\omega^2)g_{\rm fit}(\tilde{r}_{\rm t}) \right], \tag{35}$$

where $\tilde{r}_{\rm t}$ is given by

$$\tilde{r}_{\rm t} = 3.5 \left(\frac{4 - \kappa^2/\omega^2}{2} \right)^{-1/3} \left(\frac{M_{\rm i}}{2 \times 10^4 M_\odot} \right)^{1/3} \left(\frac{R_{\rm g}}{1\rm kpc} \right)^{2/3} \left(\frac{v_{\rm c}}{200\rm km/s} \right)^{-2/3} \left(\frac{r_{\rm h}}{3\rm pc} \right)^{-1}. \tag{36}$$

Here we use the N-body time unit is $t_{\rm nu} \sim r_{\rm h,i}^{3/2}/G^{1/2}M_{\rm i}^{1/2}$, and the initial tidal radius and half-mass relaxation time are, respectively, expressed as equation (3) and (24).

We set our Galaxy as a model of the parent galaxies, and set to have the constant circular velocity of 200 km/s, such that $\kappa^2/\omega^2 = 2$ and $v_{\rm c} = 200$ km/s. The average mass of the cluster stars is set to be $0.3M_\odot$.

Solid curves in figure 14 shows the mass-loss timescale of clusters as a function of their initial half-mass radii, $r_{\rm h,i}$. The initial total mass of the clusters, $M_{\rm i}$, are indicated in each panel. The distances of the clusters from the center of the parent galaxy, $R_{\rm G}$, are described beside each curve. The dotted lines show twenty times the initial half-mass relaxation time. The dashed lines indicate the Hubble time, 10^{10} years. The kink of each curve around the peak of the mass-loss timescale is due to the discontinuity of the step function, $g(\tilde{r}_{\rm t})$.

As seen in figure 14, the mass-loss timescale of clusters is proportional to their initial half-mass relaxation time, if their half-mass radii are sufficiently small. When the half-mass radii are larger than a critical half-mass radius, the mass-loss timescale of clusters becomes smaller as their half-mass radii become larger. This is because the tidal field produced by their parent galaxy strongly affects the mass loss of the clusters. The critical half-mass radius is larger as the distance of the cluster from the center of the parent galaxy is larger, i.e. the tidal field is weaker.

Figure 15 shows the properties of the galactic globular clusters: their half-mass radii and their distances from the galactic center, which are obtained from Harris (1996). We divide the galactic globular clusters by their luminosities: absolute visual magnitude $M_{\rm v} < -7$ (filled circles) and $M_{\rm v} > -7$ (open circles). The mass of a cluster with absolute visual magnitude $M_{\rm v} = -7$ is about $10^5 M_\odot$, since the solar absolute visual magnitude is $M_{\rm v} \sim 5$, and the mass-to-light ratio of the globular clusters is about 2. The dashed curves show parameters of clusters whose lifetimes are the Hubble time, derived from our evaluation formula (35). The values beside the dashed curves indicate the masses of the clusters.

Both clusters with absolute visual magnitude $M_{\rm v} < -7$ and $M_{\rm v} > -7$ are absent above the upper limit of the initial half-mass radius in the case of a cluster mass $10^5 M_\odot$. The clusters with absolute visual magnitude $M_{\rm v} < -7$ may be absent from the beginning. We can say that our upper limit of the initial half-mass radii is in a good agreement with those of the galactic globular clusters in a wide range of the distance from the galactic center, $R_{\rm G} = 1$ - 100 kpc.

The globular clusters with half-mass radii less than their lower limit in the case of cluster mass $10^6 M_\odot$ (1 pc) are absent. This is consistent with the fact that most globular clusters have mass less than $10^6 m_\odot$. However, many

clusters with absolute visual magnitude $M_{\rm v} > -7$, whose masses are less than $10^5 M_\odot$, have half-mass radii less than their lower limit in the case of cluster mass $10^5 M_\odot$, ~ 2 pc. We may interpret that these clusters initially have larger mass than $10^5 M_\odot$, suffer mass loss strongly, and become small, as seen nowadays.

6.   Summary

We investigate mass loss of star clusters in a tidal field of parent galaxy with different mass density profiles. We find that orbit families are different among parent galaxy with different mass density profiles. A fraction of regular orbits increases in the orbit family as the mass density profile of the parent galaxy is shallower. The tendency is strong in nearly planar orbits. The difference of the orbit families affects the distribution of escape time delay in each parent galaxy model. The escape time delay becomes larger as the mass density profile of the parent galaxy is shallower.

We conform that the difference of escape time delay affects mass-loss timescale of clusters with two kinds of size of tidal radii. The mass-loss timescale of clusters becomes larger as the mass density profile of the parent galaxy becomes shallower. In a moderate tidal radius, $r_{\rm t,i}/r_{\rm kg} = 1.0$, the clusters in parent galaxy with the three shallower mass density profiles ($\kappa^2/\omega^2 = 2, 2.5, 3$) have larger mass-loss timescale than those in the parent galaxy with the steepest one ($\kappa^2/\omega^2 = 1$) by 20 %, 50 % and a factor of 2.5, respectively. In the case of larger tidal radius, $r_{\rm t,i}/r_{\rm kg} = 2.2$, the difference is smaller and the largest is 60 %, which is comparison between $N = 128$ clusters in parent galaxy with the steepest and the shallowest mass density profiles.

The important result is that orbital family is attributed to the difference of the mass-loss timescales among star clusters in parent galaxy with different mass density profiles. Even if potential escapers occupy the same phase space among different parent galaxy models, the orbits and the escape time delays may be different by an order of magnitudes. Thus, the difference of mass-loss timescale among different parent galaxies is not represented by orbit-averaged method, such as Fokker-Planck simulations. Orbit-averaged methods use escape criterion based on phase space of cluster stars, for example energy and angular momentum.

We derive formula for the mass-loss timescale of clusters, as seen in equation (28). Our formula can explain a property of the population of the galactic globular cluster that their half-mass radii become smaller as their distances from the galactic center become smaller.

Acknowledgment

References

Ambartsumian, V. A. 1938, Ann. Leningrad State Univ., 22, 19
Barnes, J., & Hut, P. 1986, Nature, 324, 446
Baumgardt, H. 2001, MNRAS, 325, 1323
Baumgardt, H., & Makino, J. 2003, MNRAS, 340, 227
Binney, J., & Tremaine, S. 1987
Capuzzo Dolcetta, R., Di Matteo, P., & Miocchi, P. 2005, AJ, 129, 1906
Combes, F., Leon, S., & Meylan, G. 1999, A&A, 352, 149
Dehnen, W., Odenkirchen, M., Grebel, E. K., & Rix, H. 2004, AJ, 127, 2753
Fukushige, T., & Heggie, D. C. 1995, MNRAS, 276, 206
Fukushige, T., & Heggie, D. C. 2000, MNRAS, 318, 753 (FH)
Fukushige, T., & Suto, Y. 2001, ApJ, 557, 11
Giersz, M., & Heggie, D. C. 1994, MNRAS, 268, 257
Harris, W. E. 1996, AJ, 112, 1487
Heggie, D. C., Giersz, M., Spurzem, R., & Takahashi, K. 1998, in Highlights of Astronomy, 11A, ed. J. Andersen (Dordrecht: Kluwer Academic Publishers), 591
Heggie, D. C., & Mathieu, R. D. 1986, in Lecture Notes in Physics Vol. 267, ed. P. Hut & S. McMillan (Berlin: Springer-Verlag), 233

Kawai, A., Fukushige, T., Makino, J., & Taiji, M. 2000, PASJ, 52, 659
King, I. R. 1966, AJ, 71, 64
MacKay, R. S. 1990, Phys. Lett. A, 145, 425
McMillan, S., & Hut, P. 1994, ApJ, 427, 793
Moore, B. 1996, ApJ, 461, L13
Portegies Zwart, S. F., Makino, J, McMillan, S. L. W., & Hut, P. 2001a, ApJ, 546, L101
Portegies Zwart, S. F., McMillan, S. L. W., Hut, P., Makino, J. 2001b, MNRAS, 321, 199
Portegies Zwart, S. F., Makino, J., McMillan, S. L. W., Hut, P. 2002, ApJ, 565, 265
Portegies Zwart, S. F., McMillan, S. L. W., Gerhard, O. 2003, ApJ, 593, 352
Press, W. H., Teukolsky, S. A., Veterling, W. T., & Flannery, B. P. 1992, Numerical Recipes (Cambridge:Cambridge University Press), ch.15
Spitzer, L. 1940, MNRAS, 100, 396
Spitzer, L. 1987, Dynamical Evolution of Globular Clusters (Princeton:Princeton University Press), ch.2
Tanikawa, A., & Fukushige, T. 2005, PASJ, 57, 155 (paper I)
Trenti, M., Heggie, D. C., & Hut, P. 2007, MNRAS, 374, 344
Yim, K., & Lee, H. M. 2002, J. of Korean Astron. Soc. 35, 75

Table 2. Initial models.

$r_{t,i}$	$r_{t,i}/r_{kg}(W_0=3)$	κ^2/ω^2	κ^2	ω^2	$\rho(R)$	N
3.13	1.0	1	0.011	0.011	$\rho \propto R^{-\infty}$	$128 - 131072$
3.13	1.0	2	0.033	0.016	$\rho \propto R^{-2}$	$128 - 131072$
3.13	1.0	2.5	0.054	0.022	$\rho \propto R^{-1.5}$	$128 - 32768$
3.13	1.0	3	0.098	0.033	$\rho \propto R^{-1}$	$128 - 32768$
6.97	2.2	1	0.00098	0.00098	$\rho \propto R^{-\infty}$	$128 - 131072$
6.97	2.2	2	0.0029	0.0015	$\rho \propto R^{-2}$	$128 - 131072$
6.97	2.2	2.5	0.0049	0.0020	$\rho \propto R^{-1.5}$	$128 - 32768$
6.97	2.2	3	0.0088	0.0029	$\rho \propto R^{-1}$	$128 - 32768$

Table 3. Case of $r_{t,i}/r_{kg} = 1.0$. Phase space flux per unit energy, $\mathcal{F}$, phase space volume per unit energy, $\mathcal{V}$ in $\hat{E}_{pot,i} = 0.03$ and timescale of phase space flux, t_{ph}.

κ^2/ω^2	$\mathcal{F}$	$\mathcal{V}$	t_{ph}
1	0.108	317	2940
2	0.102	311	3050
2.5	0.0969	305	3150
3	0.0885	296	3340

Table 4. Maximum deviation of t_{mloss} for $N \leqq 8192$.

		$\left(r_{t,i}/r_{kg}, \kappa^2/\omega^2\right)$							
		$(1.0,1)$	$(1.0,2)$	$(1.0,2.5)$	$(1.0,3)$	$(2.2,1)$	$(2.2,2)$	$(2.2,2.5)$	$(2.2,3)$
	128	32	32	39	42	40	110	71	154
	256	20	22	22	39	65	115	104	86
	512	19	13	100	63	90	229	61	115
N	1024	108	67	42	105	38	189	101	182
	2048	40	54	39	42	230	130	99	158
	4096	81	53	58	238	194	248	193	227
	8192	166	58	130	133	118	362	122	–

Table 5. Our simulation results used for our fitting formula

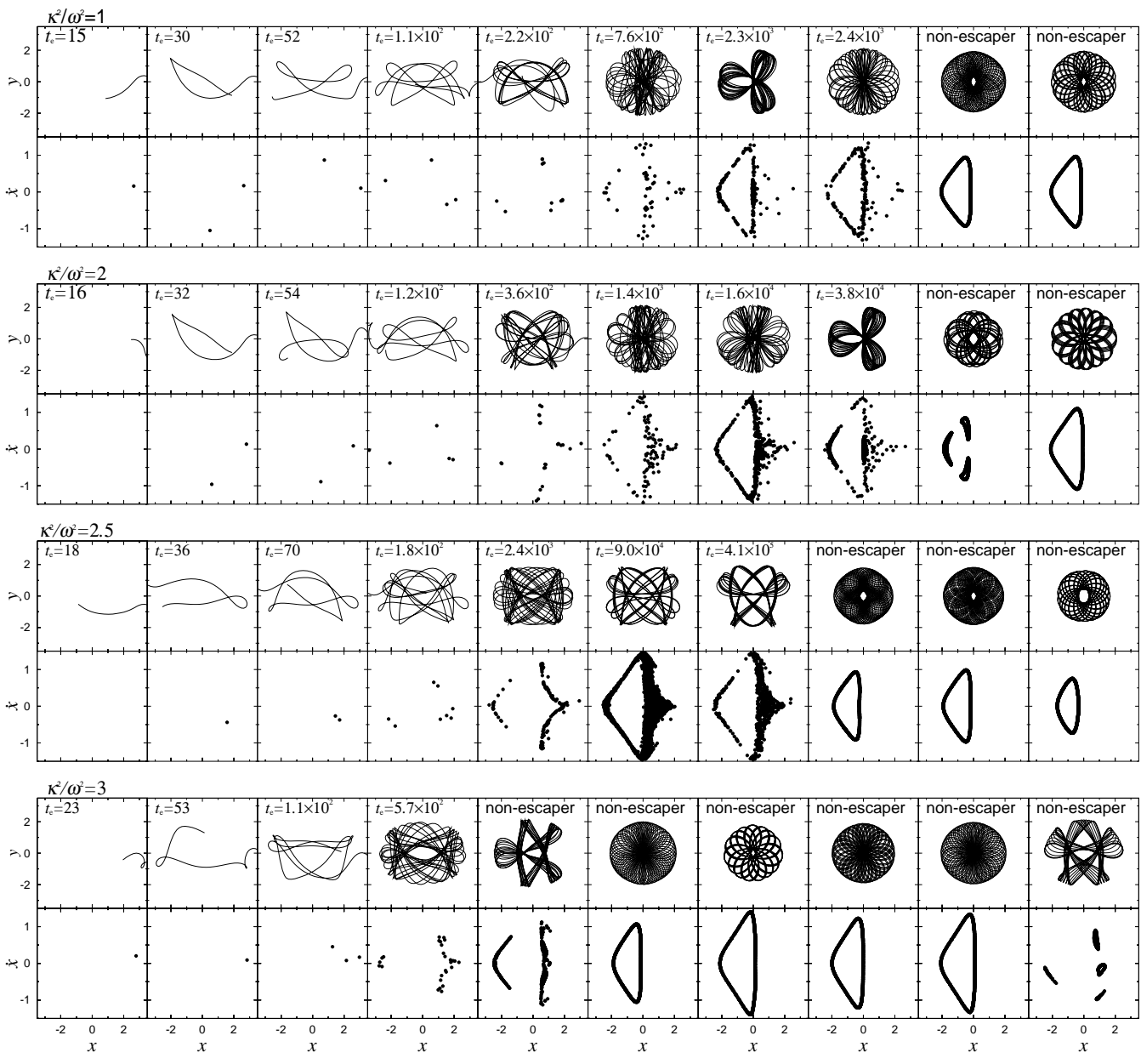| $\tilde{r}_t$	κ^2/ω^2	$t_{1000}(\tilde{r}_t)$	$x(\tilde{r}_t)$	$1 + f(\kappa^2/\omega^2)g(\tilde{r}_t)$	Ref.
3.1	1.0	800	0.4	1.0	Paper I
3.9	1.0	2000	0.75	1.0	Paper I
5.0	1.0	5000	0.85	1.0	Paper I
8.5	1.0	12000	0.9	1.0	Paper I
17	1.0	20000	0.9	1.0	Paper I
3.9	2.0	-	-	1.24	This paper
3.9	2.5	-	-	1.51	This paper
3.9	3.0	-	-	2.52	This paper
8.5	2.0	-	-	1.04	This paper
8.5	2.5	-	-	1.07	This paper
8.5	3.0	-	-	1.13	This paper

Fig. 1. Sets of orbits and surfaces of section of potential escapers. We present the orbits of the potential escapers only at $t < 5 \times 10^2$, and surfaces of section of the potential escapers until $t < 10^6$. In the surfaces of section, points represent the phase space $(x; \dot{x})$ of the potential escapers when they cross x axis in the direction of $\dot{y} > 0$. In each model, they are arrayed in small order of escape time delay from left to right.
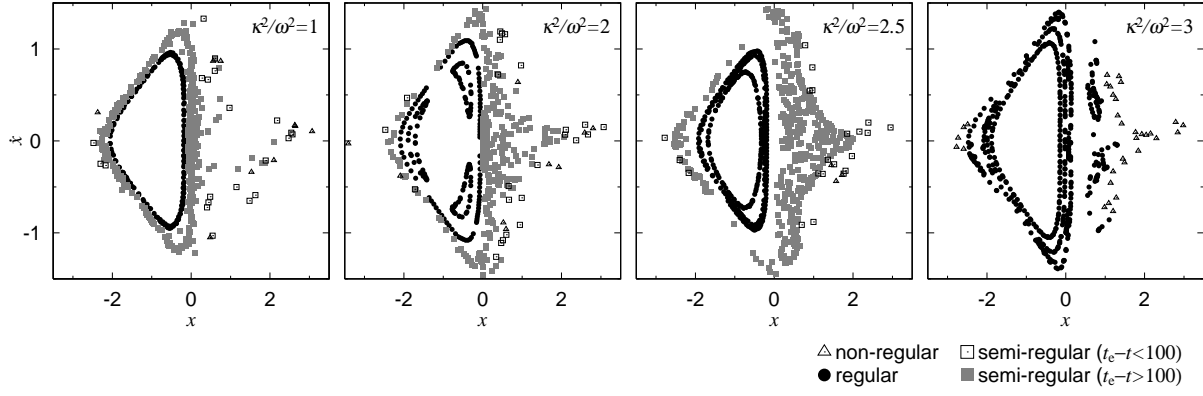
Fig. 2. For each model, surfaces of section in figure 1 are put together. Surface of section is divided into four kinds, regular orbit (black circle), non-regular orbit (triangle), and semi-regular orbit (gray and white squares). The colors of the squares are divided, whether the potential escapers cross x axis in the direction of $\dot{y} > 0$ less (white) or more (gray) than 100 time units before escape.
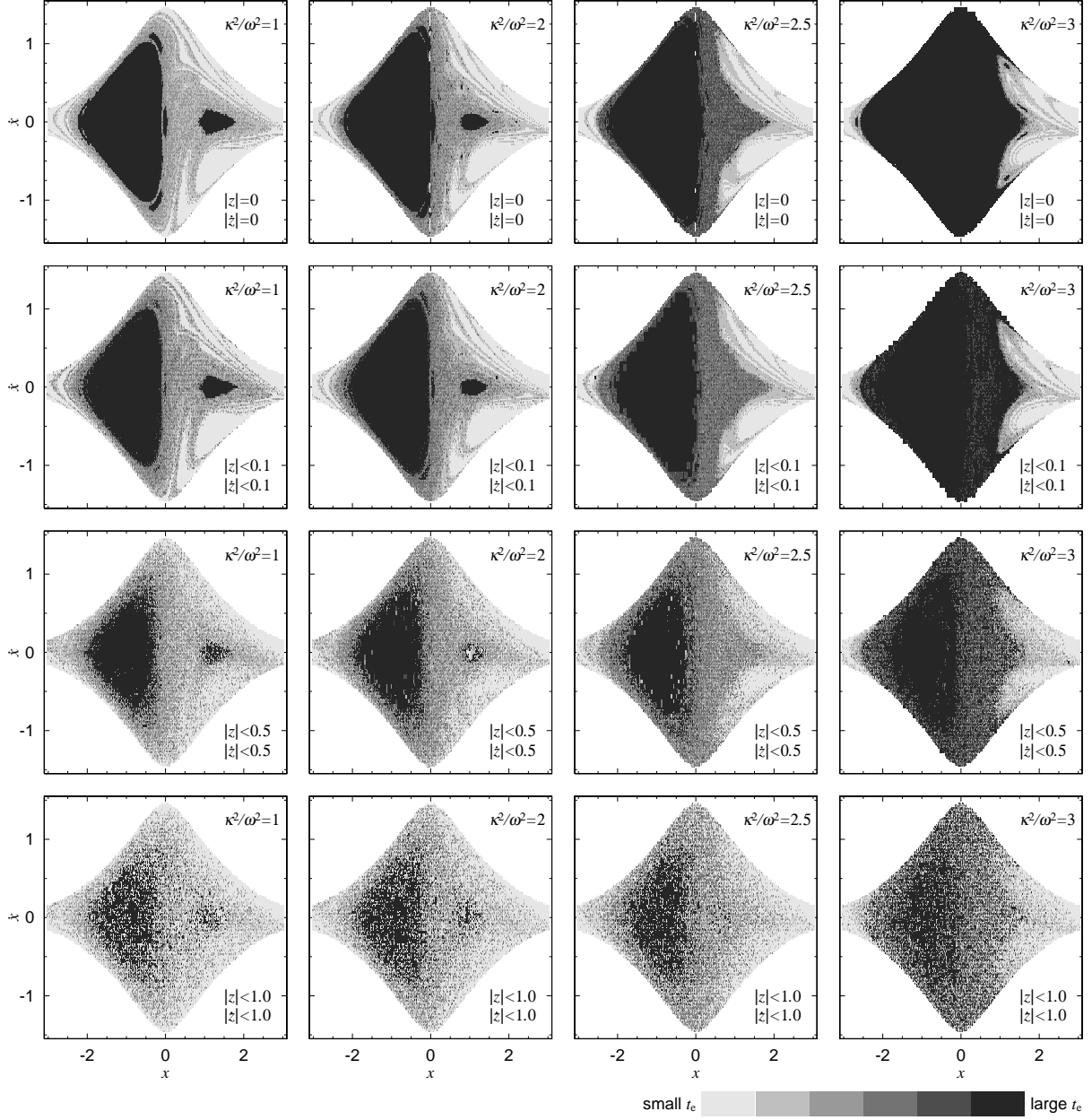
Fig. 3. Escape time delay of potential escapers as a function of their initial phase space $(x, \dot{x})$. The color of initial phase space in each panel becomes deep from gray to black in order of escape time delay, $t_e < 10^2$, $10^2 < t_e < 10^3$, $10^3 < t_e < 10^4$, $10^4 < t_e < 10^6$, and non-escaper. The conditions about $|z|$ and $|\dot{z}|$ show initial phase space of potential escapers, and their $(z, \dot{z})$ is distributed in the range at random.
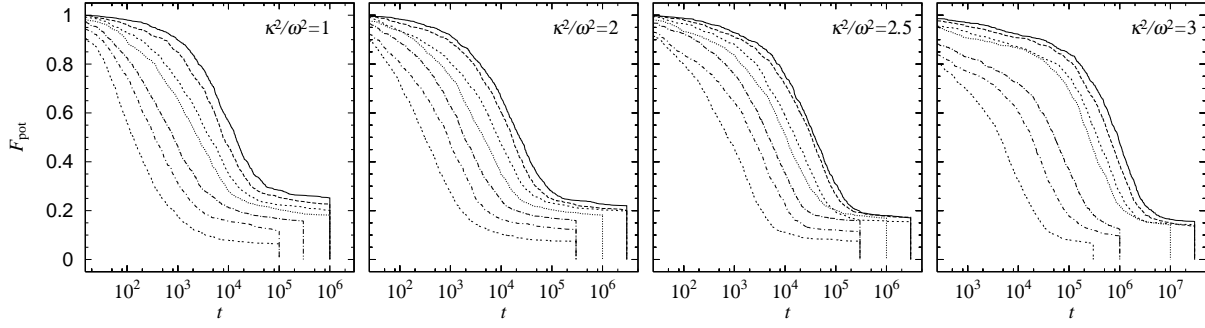
Fig. 4. Distribution of escape time delay of potential escapers. Mass density profile of parent galaxy becomes shallower from left panel to right one. In each panel, the potential escapers have, from left to right, relative energy excess $\hat{E}_{\mathrm{pot},i} = 0.24, 0.16, 0.12, 0.08, 0.06, 0.04$ and 0.03.
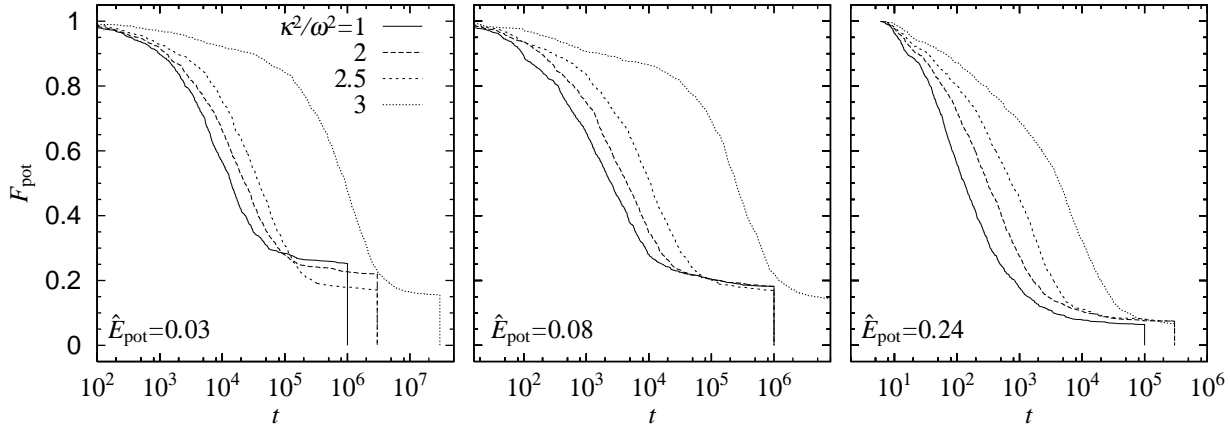
Fig. 5. Distribution of escape time delay of potential escapers. Relative energy excesses of potential escapers are $0.03, 0.08$ and 0.24, from left panel to right one.
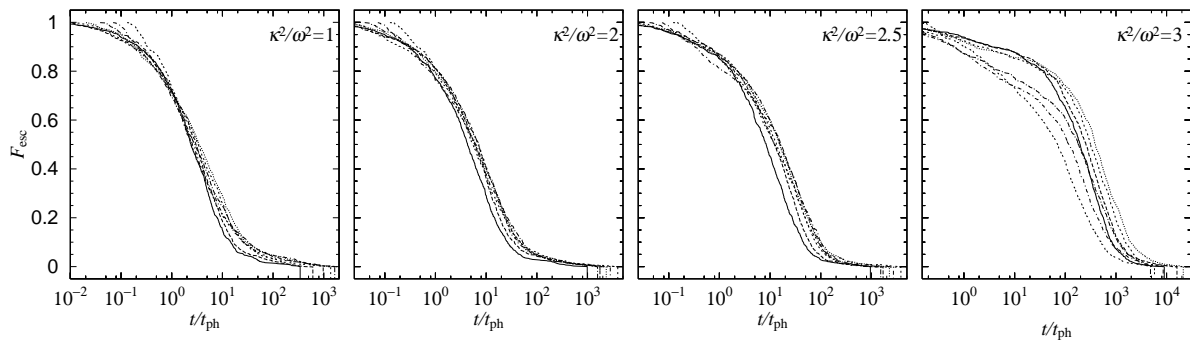
Fig. 6. Fractions of escapers which do not escape at a given time scaled by timescale of phase space flux, t_{ph}. Mass density profile of parent galaxy becomes shallower from left panel to right one.
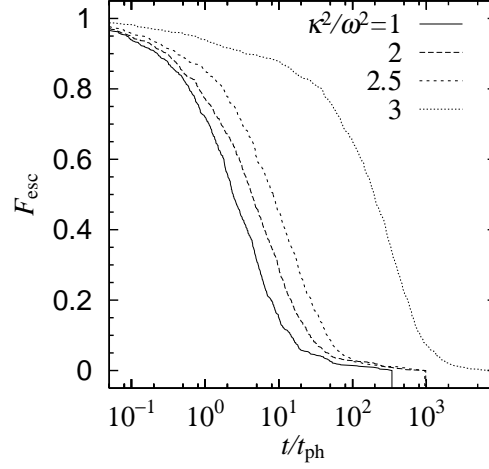
Fig. 7. Fraction of escapers which do not escape at a given time scaled by timescale of phase space flux, $t_{\rm ph}$. The escapers have the relative energy excess $\hat{E}_{{\rm pot},i} = 0.03$.
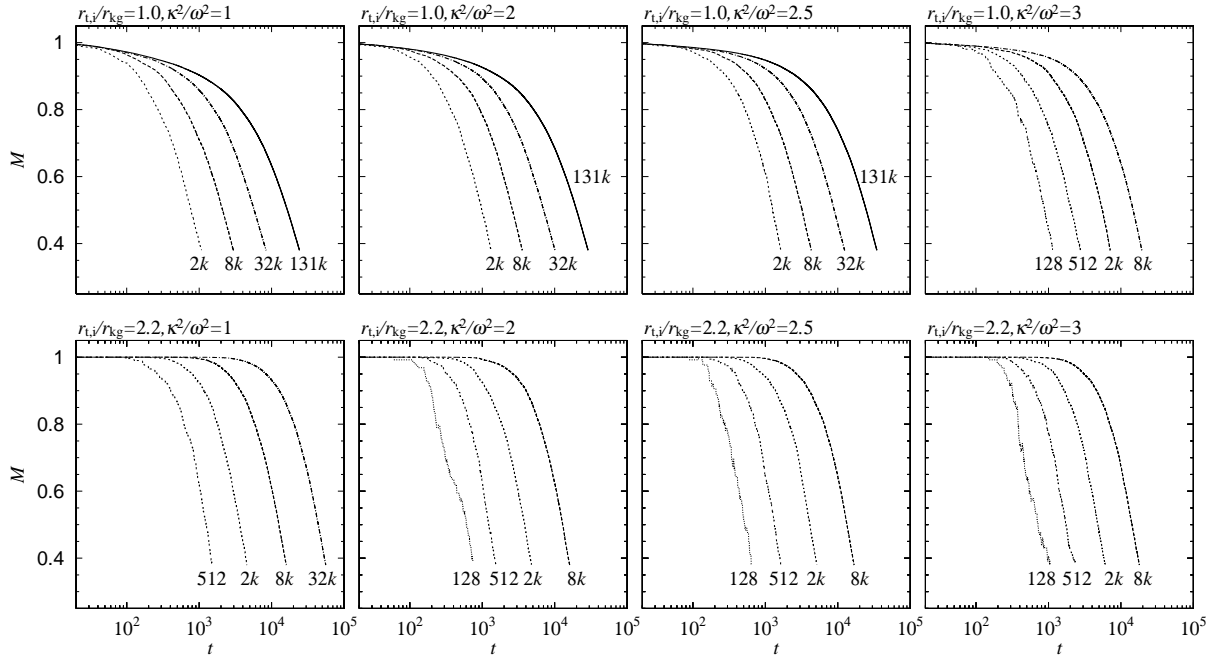
Fig. 8. Evolution of cluster masses. We show an initial tidal radius of each cluster, $r_{\rm t}/r_{\rm kg}$, and steepness of mass density profile of each galaxy, κ^2/ω^2, outside each panel. The numbers under the curves indicate the numbers of particles, N.
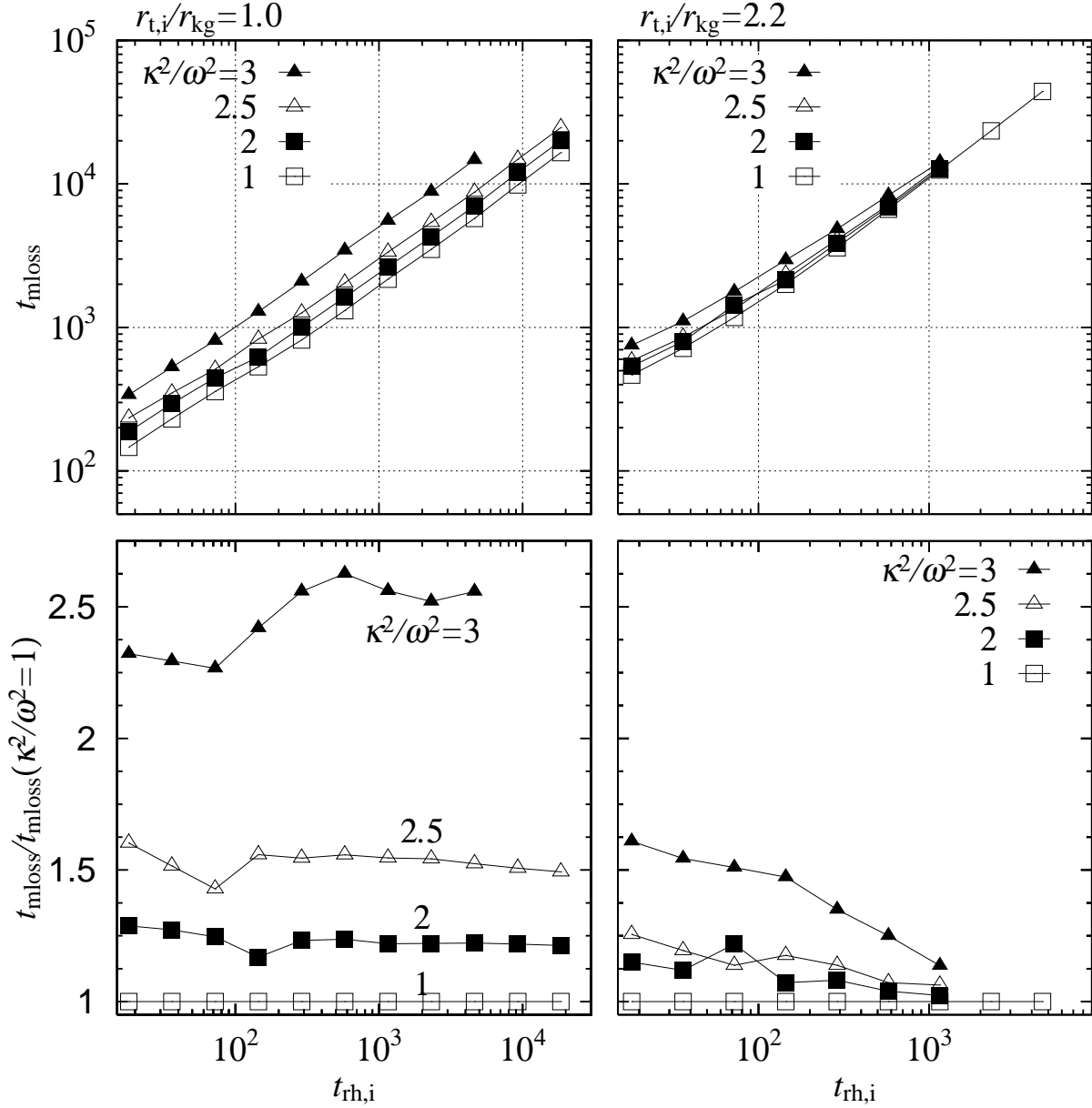
Fig. 9. Upper panels: mass-loss timescale of clusters as a function of initial half-mass relaxation time. Lower panel: mass-loss timescale of clusters scaled by mass-loss timescale of clusters in the parent galaxy with the steepest mass density profile ($\kappa^2/\omega^2 = 1$) as a function of the initial half-mass relaxation timescale.
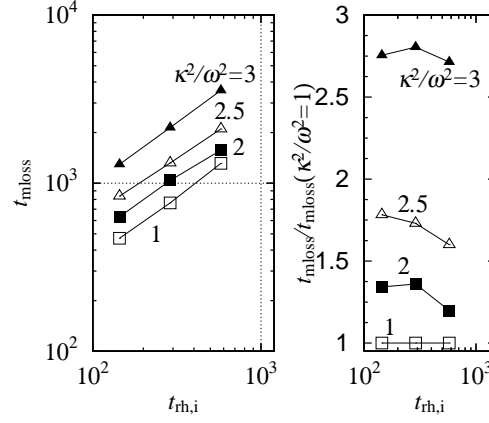
Fig. 10. Mass-loss timescale of clusters tidally unlocked as a function of initial half-mass relaxation time (left panel). Mass-loss timescale of clusters tidally unlocked scaled by mass-loss timescale in which parent galaxy have the steepest mass density profile.
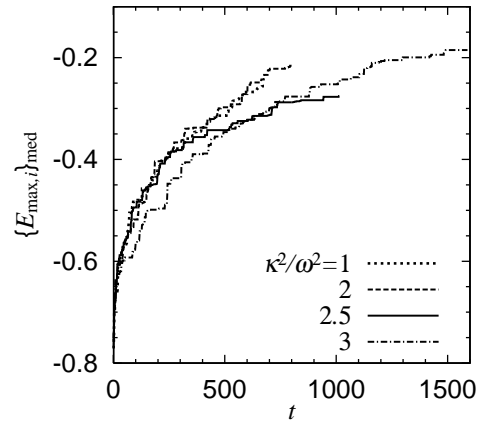
Fig. 11. Time evolution of the energy of an individual star (the definition is in the text) for clusters ($N = 1024$) in a moderate tidal radius, $r_{t,i}/r_{kg} = 1.0$. The dotted lines indicates the time evolution of the escape energy of clusters in parent galaxy with mass density profile in order of steepness from top to bottom.
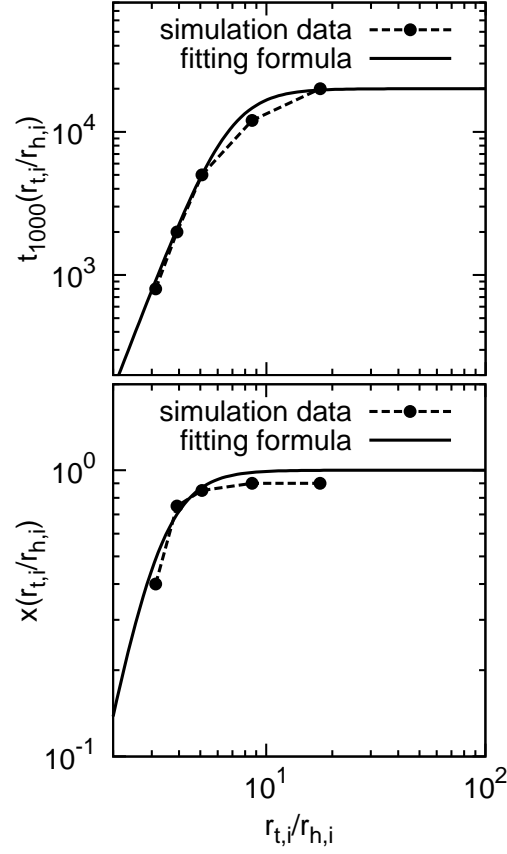
Fig. 12. Upper panel: mass-loss timescale of a cluster whose initial half-mass relaxation time is 1000 N-body unit as a function of the ratio of the initial tidal radius to the half-mass radius, $\tilde{r}_{\mathrm{t}}$. Lower panel: logarithmic slope, x $[\equiv d\ln(t_{\mathrm{mloss}})/d\ln(t_{\mathrm{rh,i}})]$, as a function of $\tilde{r}_{\mathrm{t}}$. The filled circles indicate the data points of our simulation results in paper I, and the solid curves show the fitting formula.
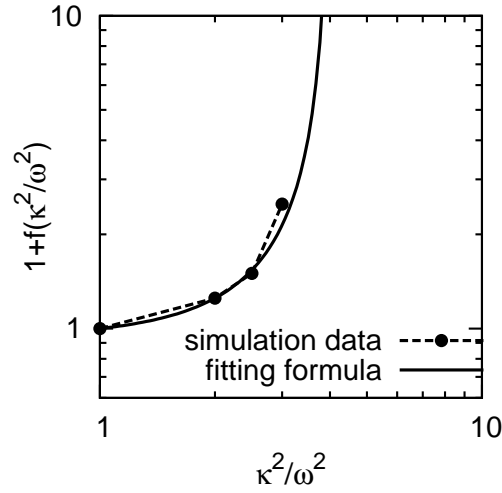

Fig. 13. Increment of mass-loss timescale, $1 + f(\kappa^2/\omega^2)$, as a function of mass density profile (κ^2/ω^2) with respect to the steepest one $(\kappa^2/\omega^2 = 1)$. The filled circles indicate the data points of our simulation results in the lower left panel of figure 9, and the solid curves show the fitting formula.
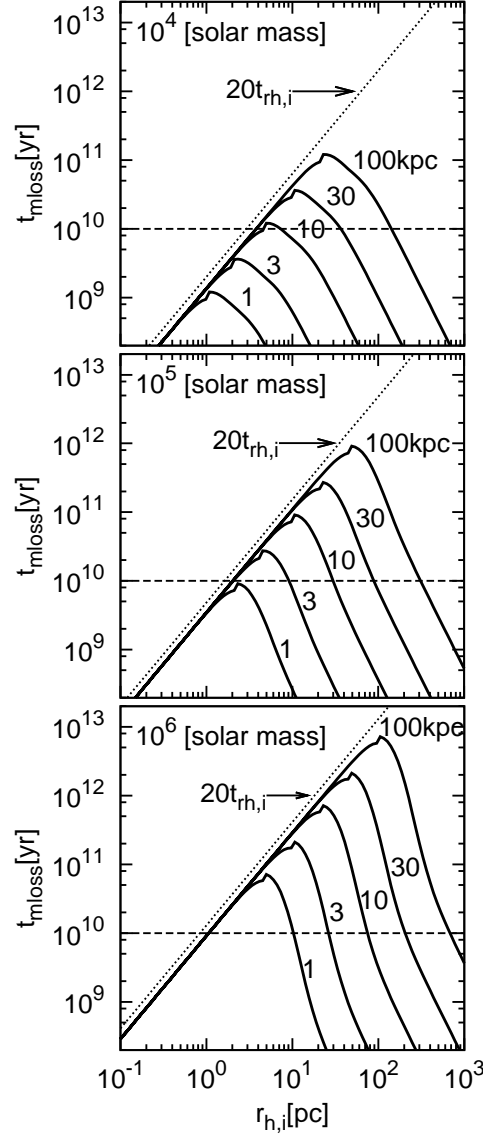
Fig. 14. Mass-loss timescale of clusters as a function of their half-mass radii, $r_{h,i}$. The initial cluster mass, M_i, is written on the top left side of each panel. The value beside each curve indicates the distance of the cluster from the galaxy center, R_g. The dotted lines show twenty times their initial half-mass relaxation time, $t_{rh,i}$. The dashed lines indicate the Hubble time, 10^{10} years.
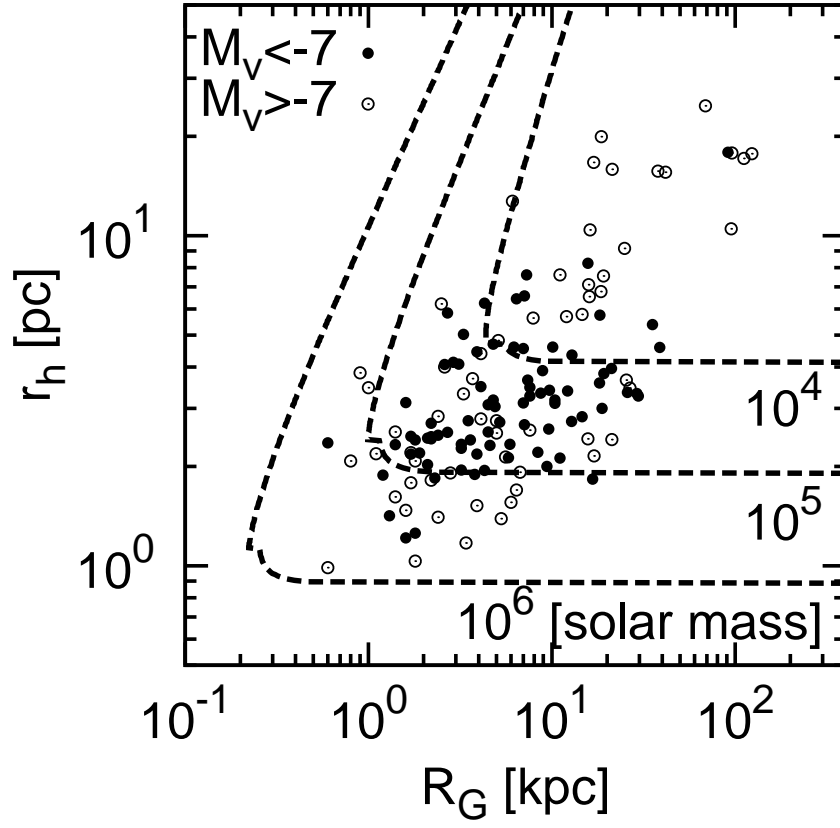
Fig. 15. Half-mass radii of the galactic globular clusters, and their distance from the galactic center, obtained from Harris (1996). The clusters are divided by their luminosities: absolute visual magnitude $M_v < -7$ (filled circles) and $M_v > -7$ (open circles).